





Coherent terahertz radiation with 2.8-octave tunability through chip-scale photomixed microresonator optical parametric oscillation

Received: 18 December 2021

Accepted: 12 August 2022

Published online: 31 August 2022


 Check for updates

Wenting Wang^{1,5} , Ping-Keng Lu^{2,5}, Abhinav Kumar Vinod¹, Deniz Turan², James F. McMillan¹, Hao Liu¹ , Mingbin Yu^{3,4}, Dim-Lee Kwong⁴, Mona Jarrahi²  & Chee Wei Wong¹ 

High-spectral-purity frequency-agile room-temperature sources in the terahertz spectrum are foundational elements for imaging, sensing, metrology, and communications. Here we present a chip-scale optical parametric oscillator based on an integrated nonlinear microresonator that provides broadly tunable single-frequency and multi-frequency oscillators in the terahertz regime. Through optical-to-terahertz down-conversion using a plasmonic nanoantenna array, coherent terahertz radiation spanning 2.8-octaves is achieved from 330 GHz to 2.3 THz, with ≈ 20 GHz cavity-mode-limited frequency tuning step and ≈ 10 MHz intracavity-mode continuous frequency tuning range at each step. By controlling the microresonator intracavity power and pump-resonance detuning, tunable multi-frequency terahertz oscillators are also realized. Furthermore, by stabilizing the microresonator pump power and wavelength, sub-100 Hz linewidth of the terahertz radiation with 10^{-15} residual frequency instability is demonstrated. The room-temperature generation of both single-frequency, frequency-agile terahertz radiation and multi-frequency terahertz oscillators in the chip-scale platform offers unique capabilities in metrology, sensing, imaging and communications.

Terahertz radiation, typically referred to frequencies from 300 GHz to 10 THz ($\lambda \approx 30\text{--}1000\ \mu\text{m}$), has spurred remarkable advances in condensed matter physics, biology and medical sciences, global environmental monitoring, metrology, information and communications technology. To achieve high frequency resolution (MHz or lower) and broad bandwidth (100 GHz or more) requirements simultaneously for frequency-agile imaging, communications, metrology, and spectroscopy applications, both widely tunable continuous-wave (CW) terahertz sources as well as terahertz frequency comb sources are

demanded extensively. The current frontier techniques for the generation of tunable CW terahertz radiation include millimetre-wave oscillator frequency multiplication^{1,2}, dual infrared wavelengths photomixing^{3–6}, as well as using quantum-cascade lasers (QCLs)^{7–9}, molecular gas lasers¹⁰, and free-electron lasers¹¹. Frequency-multiplication approaches can offer milliwatt level radiation power, but hardly reach beyond 1 THz in frequency. In addition, their frequency bandwidths are often limited due to impedance matching and/or waveguide cutoff constraints.

¹Fang Lu Mesoscopic Optics and Quantum Electronics Laboratory, University of California, Los Angeles, CA 90095, USA. ²Terahertz Electronics Laboratory, University of California, Los Angeles, CA 90095, USA. ³State Key Laboratory of Functional Materials for Informatics, Shanghai Institute of Microsystem and Information Technology, Shanghai, China. ⁴Institute of Microelectronics, A*STAR, Singapore 117865, Singapore. ⁵These authors contributed equally: Wenting Wang, Ping-Keng Lu.  e-mail: wentingwang@ucla.edu; mjarrahi@ucla.edu; cheewei.wong@ucla.edu

Photonics paves the way to the realization of reliable high-frequency terahertz radiation sources. Notably, much recent progress is offered by the development of terahertz QCLs based on inter-miniband transitions within the conduction band of semiconductor heterostructures. Several realizations of tunable QCLs have been recently demonstrated by intracavity difference-frequency generation^{12,13}, microelectromechanical-based transverse mode manipulation¹⁴, and metasurface-based vertical-external-cavity surface emission¹⁵. Nevertheless, their practical application is often limited by low duty cycle (quasi-CW) operation, restricted frequency tuning range, and the need for cryogenic cooling. Aside from QCLs, a widely tunable terahertz gas laser based on discrete rotational transitions of molecular gas was recently demonstrated with CW operation¹⁰. However, apart from a relatively larger system footprint due to the required vacuum pump and pressure control elements, its emission frequencies have not surpassed 1 THz so far. Photomixing, which is by far the most reliable technique to achieve wide frequency tunability, CW generation and room temperature operation, is the process of converting a pair of beating optical waves into terahertz radiation at their frequency difference¹⁶. Unlike nonlinear difference-frequency generation, photomixing in a photoconductor does not require phase matching and its conversion efficiency is not constrained by the Manley–Rowe limit since the terahertz radiation stems from the acceleration of electron-hole pairs rather than direct photon conversion^{17,18}. Therefore, it has been widely recognized in state-of-the-art terahertz generation for frequency-domain spectroscopy^{19,20} and communication systems^{21,22}. Furthermore, terahertz frequency combs have been explored for many high-resolution, high-accuracy metrology and spectroscopy applications, and the typical techniques for the generation of terahertz frequency combs include direct synthesis within QCLs²³, dispersion compensation of QCLs²⁴, down-conversion and frequency division from stabilized femtosecond mode-locked lasers via photomixing^{25,26}. Besides the QCL and mode-locked laser, a semiconductor injection laser with three different active regions is designed to obtain octave-spanning terahertz frequency combs²⁷. The demonstrated terahertz frequency combs can be challenging in terms of the system complexity, small repetition rate, and sizable footprint for cryogenic cooling, limiting some applications outside the laboratory. In parallel, microresonator-based nonlinear processes are proven to provide coherent parametric oscillation generation^{28–30}, octave-spanning spectral translation^{31,32}, and precision broadband frequency combs^{33–36} via cavity-enhanced four-wave mixing which are advancing research in laser spectroscopy³⁷, optical coherent communications³⁸, optical neural networks^{39,40}, laser ranging^{41–44}, and optical clocks^{45,46}. High-power and coherent millimeter waves are generated recently with the microresonators combining with optical frequency division, dispersion compensation, and optical spectral shaping techniques^{47,48}, but the frequency tuning range and resolution can be limited.

Here we present a coherent frequency-agile terahertz wave synthesizer with 2.8-octave tunability, sub-Hz linewidths, and 10^{-15} 1,000-sec relative frequency instabilities, capable of generating both single-frequency and multi-frequency terahertz oscillators, through a microresonator-based optical parametric oscillator integrated with a plasmonic nanoantenna array photomixer. First, multi-segmented cavity mode dispersion engineering and polarized hybrid mode interactions in the nonlinear microresonator enables the broadband $\chi^{(3)}$ optical parametric oscillation over 2.3 THz, including competition between mode-crossing Turing instabilities and Faraday instabilities. Secondly, with plasmonic photomixed optical-to-terahertz frequency division, our chip-scale platform achieves the coherent single-frequency synthesis from 330 GHz to 2.3 THz, the largest range realized to our knowledge, and with fine ≈ 27 Hz tuning steps on the terahertz carrier. The generated coherent signal has a cavity-

mode-limited frequency tuning step of ≈ 20 GHz and ≈ 10 MHz intracavity mode continuous frequency tuning range at each step. Our terahertz synthesizer does not require optical spectral shaping and, via control of the microresonator intracavity power, multi-frequency terahertz oscillators are also observed through heterodyne beat between our pump laser and the localized optical sub-comb lines. Third, with feedback stabilization of the microresonator intracavity power, we observed less than 100 Hz linewidths on the terahertz radiation, bounded only by the instrument limits. With dual-stage pump power- and frequency-stabilization, the long-term frequency stability is improved by five orders-of-magnitude, reaching an instrument-limited frequency residual instability of 1.6×10^{-15} at 1000 s averaging. The chip-scale 2.8-octave tunable synthesizer, with coherent sub-Hz linewidths and 1.6×10^{-15} frequency instabilities, at room temperature provides an alternative platform for next-generation terahertz imaging, sensing, metrology and communications.

Results

Chip-scale frequency-agile terahertz radiation synthesizer based on a nitride microresonator and a InAs nanoantenna array

A conceptual schematic of the broadly-tunable terahertz radiation synthesizer based on a dispersion-managed silicon nitride nonlinear microresonator and a plasmonic photoconductive InAs nanoantenna array photomixer is illustrated in Fig. 1a. The tunable optical parametric oscillation (OPO) generation setup is shown in inset i and potential applications of the tunable terahertz synthesizer are illustrated in inset ii. The microresonator contains seven tapered waveguide segments to engineer the dispersion with varying widths from 1 to 2.5 μm , five 180° bends and two 90° bends for a fixed silicon nitride height of 800 nm. The curved waveguides serve as mode-filters^{49,50} to maintain the fundamental transverse mode (TE₀₀ and TM₀₀) operation. The averaged cavity group velocity dispersion (GVD) of the fundamental TE and TM modes are 18.31 and 158.10 fs²/mm extracted from the cold-cavity mode spectra measured by swept-wavelength interferometry³⁶ after the mode frequency calibration (detailed in Methods and Supplementary Information I). The loaded quality factors are 1.55×10^6 (TE₀₀) and 1.23×10^6 (TM₀₀) around the pump laser mode, with mode free spectral ranges (FSR) of 19.87 and 19.72 GHz respectively. The resonant frequencies of the fundamental mode family are $\omega(\mu) = \omega_0 + D_1\mu + \frac{D_2}{2}\mu^2$ when just considering GVD, where $\omega_0/(2\pi)$ is the pump cavity mode frequency, $D_1/2\pi$ is the cavity mode FSR, μ is the azimuthal mode number with respect to the pump cavity mode, $D_2 = -c/n_0 D_1^2 \beta_2$ is the cavity mode dispersion, c is the speed of the light, n_0 is the refractive index of the nitride resonator, and β_2 is the GVD. To effectively compensate the phase mismatch $\beta_2 \Omega^2$ (Ω is the parametric oscillating frequency spacing) and $\chi^{(3)}$ Kerr nonlinear phase shift γP_{in} (γ is nonlinear coefficient and P_{in} is microresonator intracavity power) in our normal-dispersion microresonator, mode-frequency shift induced by the transverse mode interaction between our hybridized polarization orthogonal modes (TE and TM) is utilized. Figure 1b shows the computed mode interaction evolution based on the operation temperature by solving the coupled mode equations (detailed in Supplementary Information I). The target cavity mode ω_μ is split into two modes $\omega_\mu \pm \Delta\omega$, where $\Delta\omega/(2\pi) \approx \mu(D_{1\text{TE}} - D_{1\text{TM}})/2\pi + \mu^2(D_{2\text{TE}} - D_{2\text{TM}})/4\pi \approx \mu c/L(T)/(n_{\text{TE}}(T) - n_{\text{TM}}(T))/2\pi$ is the mode-shift frequency, $n_{\text{TE}}(T)$ and $n_{\text{TM}}(T)$ are the temperature-dependent refractive indexes for TE and TM modes, and $L(T)$ is the physical cavity length. Insets i, ii, and iii show the representative mode spectra at different chip temperatures, fitted to the double-Lorentzian model to obtain the mode linewidth and mode-splitting frequency.

Three modes (ω_0 , $\omega_{+\mu}$, $\omega_{-\mu}$) are involved in the excitation of the parametric oscillation. By directly modifying the frequency of the target mode through mode-shifting, the tunable phase matching

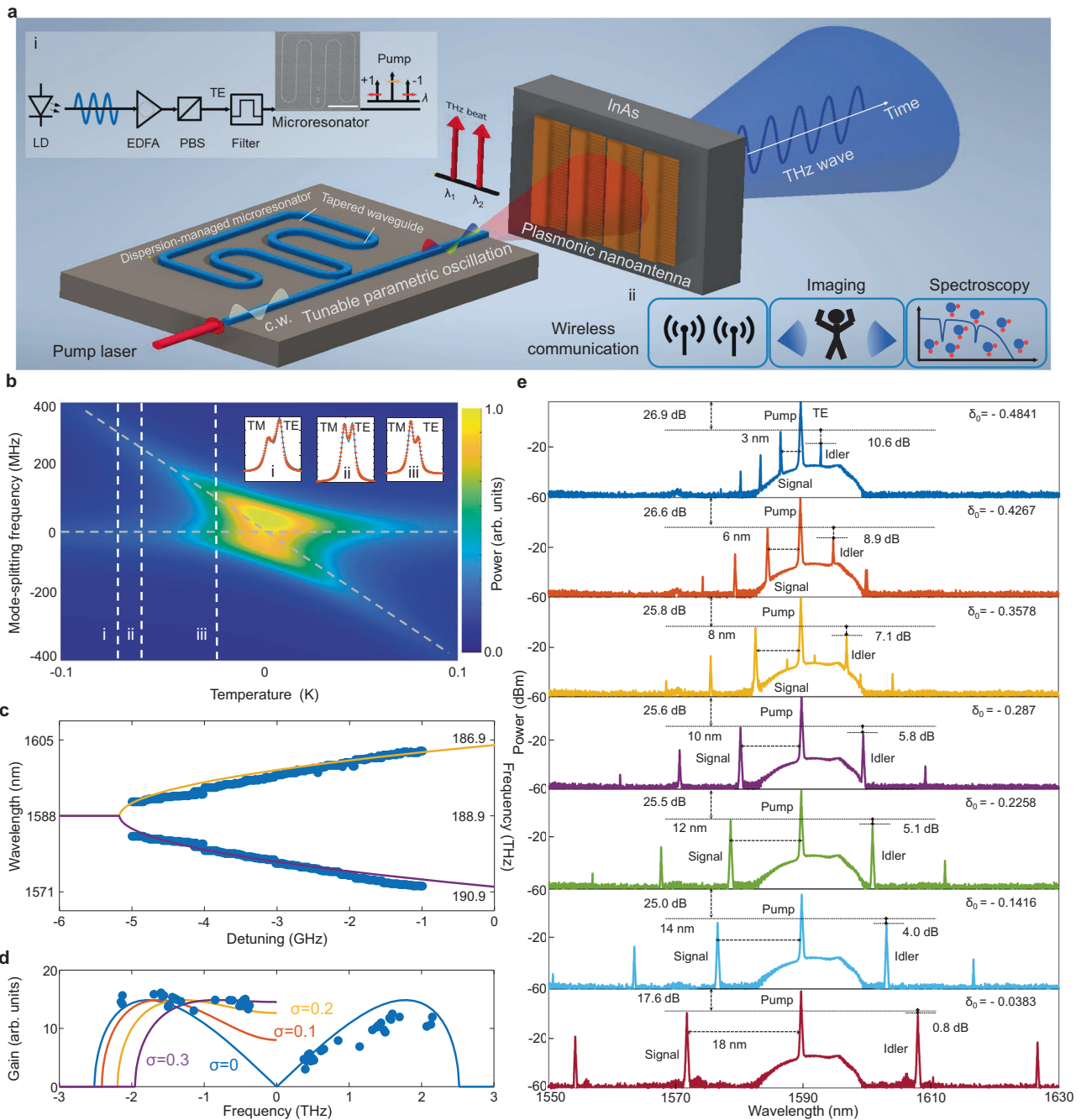


Fig. 1 | Chip-scale THz radiation source based on the high-Q dispersion-managed nitride parametric microresonator and plasmonic photoconductive InAs nanoantenna array photomixing. **a** Illustration of the coherent 2.8-octave tunable terahertz parametric radiation. Inset **i**: Tunable optical parametric oscillation generation process with microresonator. LD laser diode, EDFA erbium-doped fiber amplifier, PBS polarization beam splitter, TE transverse electric, c.w. continuous wave. Scanning electron micrograph with scale bar of 400 μm . Inset **ii**: Applications of the broadly-tunable coherent terahertz parametric radiation. **b** Modeled hybridized mode spectra evolution from the TE-TM coupled modes

with swept cavity temperatures, TM: transverse magnetic. Inset **i**, **ii**, **iii**: Measured hybridized mode spectra at different mode temperatures measured with swept-wavelength interferometry and fitted by the double-Lorentzian model. **c** Generated broadly-tunable parametric oscillation via continuously swept pump-resonance detuning. **d** Parametric gain oscillation with and without coupled-mode frequency shift, matched with the experimentally measured parametric oscillation peak power. **e** Representative microresonator tunable parametric oscillation under controlled pump-resonance detuning.

condition is obtained over a broad optical spectral range via $2\omega_0 - \omega_p - \omega_{\text{ii}} = \beta_2 \Omega^2 + \gamma P_{\text{in}} - \varphi(\omega_{\text{ii}}, T)$, where $\varphi(\omega_{\text{ii}}, T) = \beta_1(\Delta\omega/2\pi) + \beta_2 \Omega \Delta\omega / (2\pi)$ and β_1 is the group velocity. The required mode-splitting frequency is $\Delta\omega/2\pi = (\beta_2 \Omega^2 + \gamma P_{\text{in}}) / (\beta_1 + \beta_2 \Omega)$. The target mode frequency and the corresponding splitting frequency both depend on the microresonator temperature, which is related to the intracavity power $P_{\text{in}}(\delta)$ based on the pump-resonance detuning $\delta = (\omega_p - \omega_0) / (2\pi)$. Figure 1c shows the measured tunable parametric oscillation

generation via continuous pump-resonance detuning of $\delta = 4$ GHz when the resonant mode is pumped at 1588.15 nm. The resultant parametric signal sidebands tunes from 1585.4 to 1571.5 nm, corresponding to a Ω tuning from 370 GHz to 1.7 THz ($\Delta\Omega = 1.33$ THz). This specific microresonator thus offers an optical-to-terahertz tuning ratio $\chi = \Delta\Omega/\delta$ of 332.5.

Substantiating our measurements shown in Fig. 1, the $\chi^{(3)}$ phase matched parametric sideband curves are calculated based on the

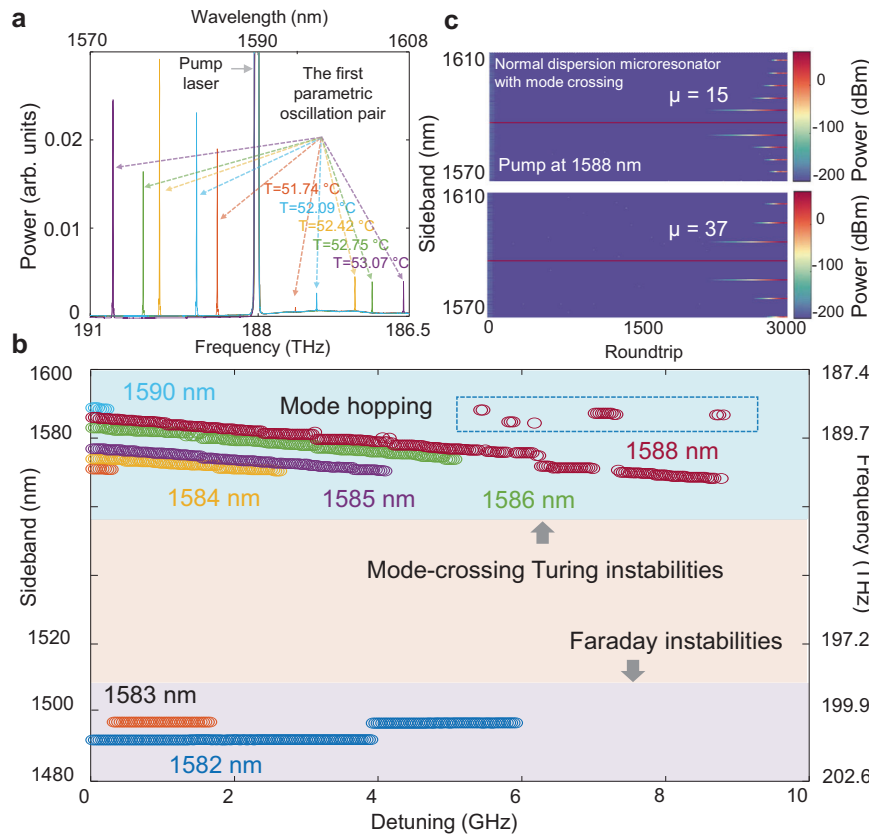


Fig. 2 | Broadly-tunable optical parametric oscillation in the dispersion-managed microresonators. **a** Measured parametric oscillation pair at different chip temperatures from 51.74 to 53.07 °C while maintaining constant pump power and optimal pump detuning to obtain the initial oscillation pair. **b** Pump wavelength dependence of parametric oscillation. Competition between different

parametric oscillations, determined by the intrinsic Faraday ripple⁵¹ and thermal-related mode frequency shift, is observed. **c** Lugiato-Lefever modelling with avoided-mode-crossings for parametric sidebands of 0.3 and 0.74 THz tunability. μ is the azimuthal mode number with respect to the pump cavity mode.

modified phase matching condition $L \frac{\beta_2}{2} \Omega^2 + 2\gamma LP_{in}(\delta)^2 - \delta - \varphi(\omega_\mu, T) = 0$ after considering the cavity boundary condition in the Lugiato-Lefever (LL) model and the thermal-mediated mode-splitting as shown in Fig. 1c with orange (idler) and purple (signal) curves. The calculated parametric sidebands are consistent with our measurements. Mode-splitting is a local effect which breaks the phase-matching symmetry of the signal ($\omega_{\pm\mu}$) and idler (ω_μ) leading to asymmetric parametric gain – Fig. 1d shows the resultant measured and calculated signal and idler peak powers. The power difference is attributed to the asymmetric parametric gain, calculated as $G = \sqrt{(\gamma P_{in})^2 - \Delta k}$, where Δk is phase mismatch. The computed parametric gain profiles are also shown in Fig. 1d where the blue curve is the calculated parametric gain profile with anomalous dispersion as a reference, and $\sigma = \delta + \varphi$ represents the extra phase mismatch in the parametric gain symmetry breaking. After adding the extra mode frequency shift $\Delta\omega/(2\pi)$, the parametric oscillation is generated at effective pump-resonance blue detuning. Figure 1e shows the representative tunable parametric oscillation at different normalized pump-resonance detunings [$\delta_0 = \delta/D_{TE}/(2\pi)$], where the power imbalance between signal and idler from 10.6 dB ($\delta_0 = -0.4841$) to 0.8 dB ($\delta_0 = -0.0383$) originates from the additional mode-frequency shift. The pump-to-signal power conversion efficiency is related to the pump-to-signal power imbalance ratio (denoted in dB in Fig. 1e) determined by the pump resonance detuning and avoided mode frequency shift. A higher pump-to-signal conversion (smaller power imbalance in dB) allows for a higher terahertz wave emission power.

Thermal and local dispersion dependences of the tunable terahertz optical parametric oscillation

Tunability of the parametric oscillation is associated with the differential TE-TM thermo-optic effects in the microresonator, demonstrated by monitoring the parametric oscillation at different operating temperatures from 51.74 to 53.07 °C for a fixed pump laser power and the same resonant mode frequency, as shown in Fig. 2a. The frequency of the initial parametric oscillation pair can be tuned over 12 nm when the temperature changes 1.3 °C. The power variation of the parametric sidebands is related to the magnitude of the $\Delta\omega/(2\pi)$. Maximizing the spectral tuning range of the parametric oscillation requires a careful selection of the pump cavity mode. By pumping the cavity modes located between 1582 to 1590 nm with a 1 or 2 nm spectral step at a fixed on-chip pump power, we examine the parametric oscillation generation dynamics. At the shorter pump wavelengths, the tunable parametric oscillation vanishes but Faraday parametric oscillation⁵¹ emerges due to the periodic dispersion design in our microresonator⁴⁹. When resonant modes at longer wavelengths are pumped, bistable switching dynamic between Faraday and Turing parametric oscillation is observed, which results from parametric gain competition between the two parametric oscillation processes⁵². The Faraday branch is induced by periodic modulation of the microresonator dispersion. The gain peak sideband frequency away from pump laser frequency is

$\omega_f = \sqrt{2 \left[\frac{(\beta_2 - 2\gamma P_{in}) \pm \sqrt{(\gamma P_{in})^2 + (\frac{\beta_2}{L})^2}}{\beta_2} \right]}$, where L is microresonator cavity length. To thoroughly denote the pump wavelength dependence, the

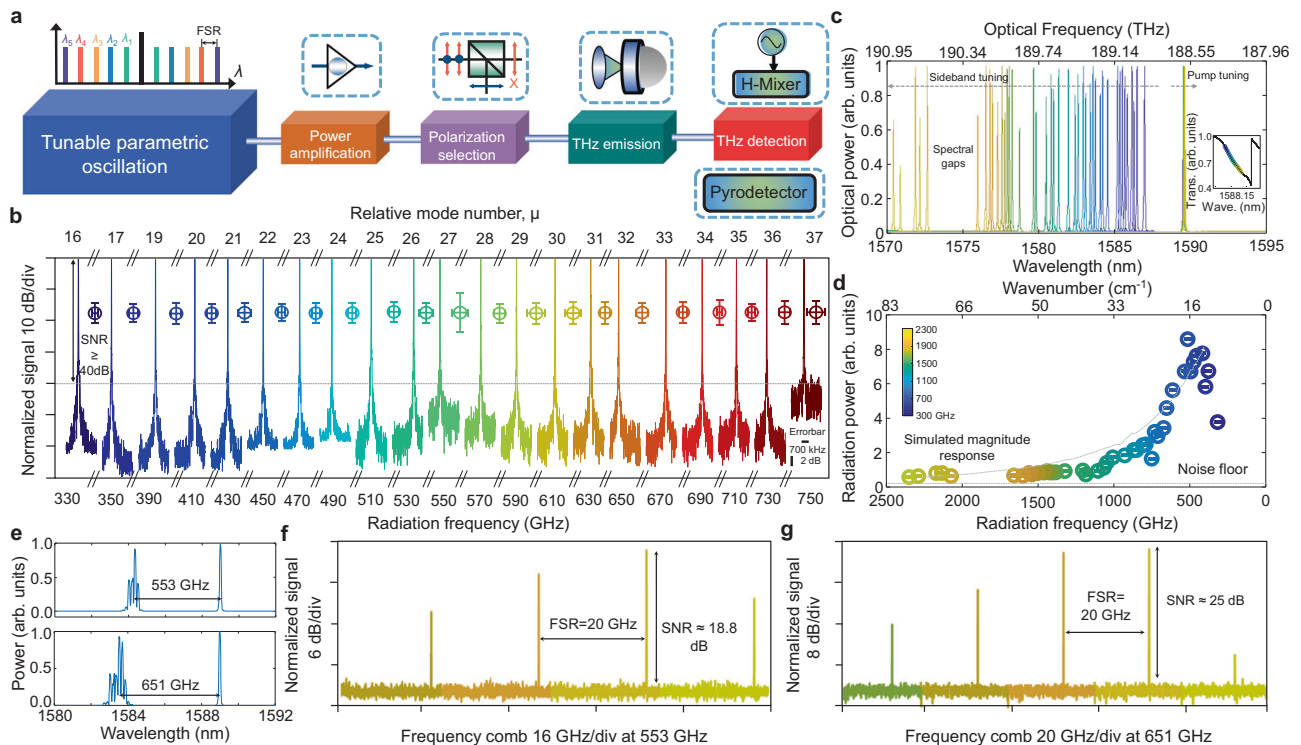


Fig. 3 | 2.8-octave tunable radiation and multi-frequency terahertz oscillators through photomixed microresonator optical parametric oscillation.

a Schematic of the terahertz generation and detection setup. FSR: Free-spectral range. **b** Measured down-converted RF spectra showing ≈ 100 kHz 3-dB instantaneous linewidth and more than 50 dB signal-to-noise ratio (SNR) (apart from the 550 and 750 GHz terahertz radiation frequencies), corresponding to generated radiation from 330 to 750 GHz. Experimental error bars for each carrier are illustrated too. **c** Measured tunable parametric sidebands via continuously smaller

pump-resonance detuning in one cavity resonance ($\mu' = 9500$). Inset: the hot cavity resonance including Kerr and thermally-induced resonance red shift (≈ 14.68 GHz) and the corresponding color-coded pump-resonance detuning. **d** Measured 2.8-octave coherent radiation power from 330 GHz to 2.3 THz with a pyroelectric detector and lock-in amplification. **e**, Measured optical spectra with sub-comb lines when optimizing the microresonator intracavity power. **f**, **g** Measured multi-frequency terahertz oscillators at center frequency of 553 and 651 GHz corresponding to the top and bottom panel of (**e**).

high frequency parametric sidebands (signal) are filtered out to highlight the frequency tuning range and parametric oscillation competition dependence on the pump-resonance detuning as shown in Fig. 2b. The frequency tuning range is highly related to the local resonant mode dispersion and thermally-mediated mode-splitting frequency shift resulting from the optical power absorption in the microresonator. Mode-hopping instabilities are also observed but these can be suppressed by optimizing the microresonator operation temperature. In support of the measurements, the LLE numerical modeling of Fig. 2c (detailed in Methods) verifies the comparative deterministic parametric oscillations when the mode frequency shifts are introduced at $\mu = 15$ and 37.

Tunable radiation and multi-frequency terahertz oscillators generation

With the designed cavity mode dispersion and differential TE-TM thermal dependence, the tunable OPO is facilitated by gradually changing the pump-resonance detuning, where the optical power absorption leads to increase (decrease) of the resonant mode temperature by forward (backward) pump wavelength tuning. The generated tunable OPO is passively down-converted to the terahertz radiation via a plasmonic nanoantenna array built on the InAs substrate⁵³. The incident optical beam excites surface plasmons on the nanoantenna array, providing strong enhancement of the generated near-field photocarriers, subsequently accelerated by the surface built-in electric field in the InAs substrate without any external bias voltage. Since the nanoantenna array operates without any bias voltage, the direct current through the emitter is eliminated, leading to minimal heating. Consequently, the shot noise and thermal noise contributed

from the nanoantenna array itself is believed to be negligible. Figure 3a illustrates the terahertz signal generation and detection schematic. By optimizing the intracavity power and detuning, terahertz radiation is generated over a broad frequency range (detailed in Methods and Supplementary Information II). To generate tunable terahertz radiation, two adjacent resonant modes ($\mu' = 9500$ and 9501, where μ' is the absolute cavity mode number) are examined and optically pumped, which is subsequently down-converted to radio frequency (RF) spectral ranges using a harmonic mixer to examine the signal-to-noise ratio (SNR), frequency tunability (intra- and inter-resonant modes), and frequency stability. The detected terahertz radiation spectra span from 330 to 750 GHz (bounded only by harmonic mixer frequency bandwidth) as shown in Fig. 3b and feature an ≈ 50 dB SNR, apart from the 550 and 750 GHz frequencies where strong water vapor absorption occurs. The fluctuations in frequency and power are included in standard deviation error bars of Fig. 3b as well. Subsequently, in Fig. 3c, we examine the terahertz frequency tuning range over a single resonant mode ($\mu' = 9500$), with tunable optical parametric sidebands covering from 1586 to 1570 nm where the spectral gaps are related to local phase mismatching of the Turing instabilities. The spectral gaps require more accurate phase matching between the pump and signal by optimizing the dispersion engineering and operating temperature. The corresponding pump laser absolute frequencies are shown in Fig. 3c inset over the thermally broadened cavity resonance. Power equalization between the pump and parametric sidebands are performed to optimize photomixing efficiency. The radiated terahertz power is measured with lock-in detection using a pyroelectric detector at a 20 Hz. Figure 3d shows the detected terahertz power across 2.8-octaves from 330 GHz to 2.3 THz, which decreases at the higher

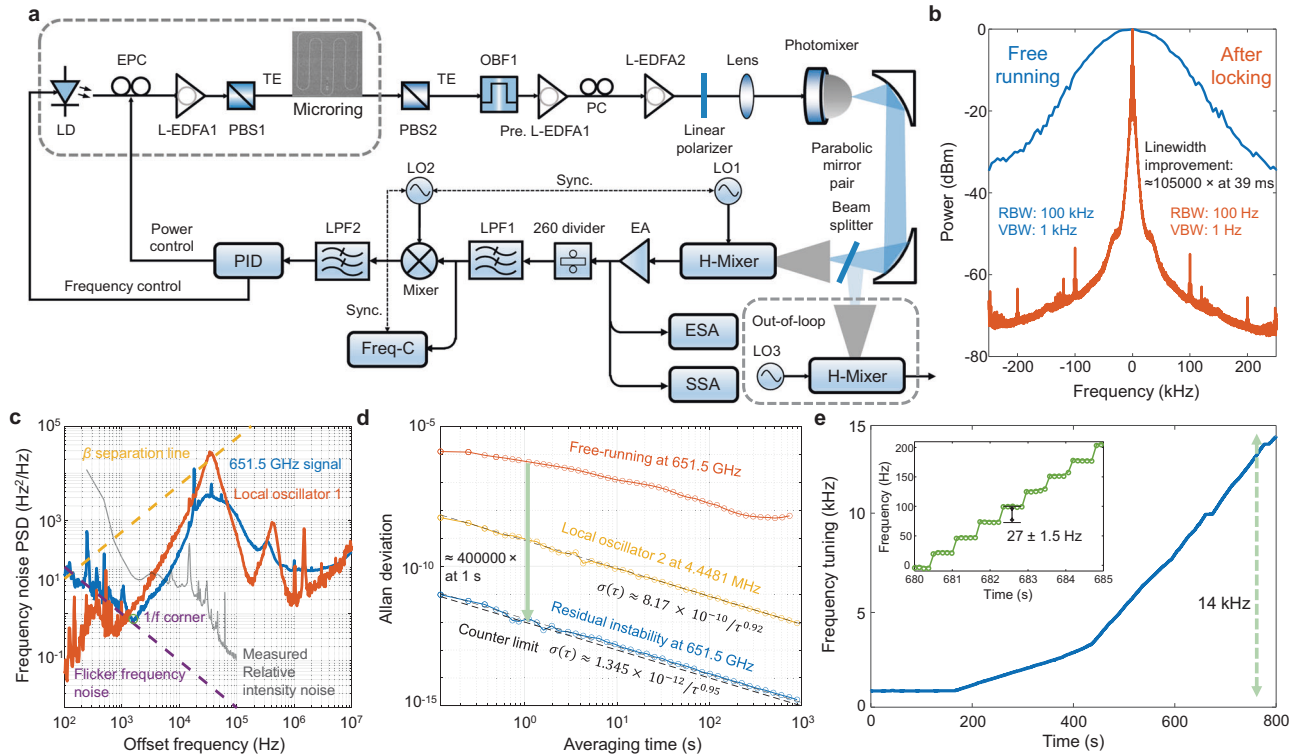


Fig. 4 | Sub-100-Hz frequency stabilization of the terahertz radiation via feedback control of the microresonator intracavity power. **a** Terahertz generation and feedback control experimental setup. EPC: electrically controlled polarization controller, OBF: optical bandpass filter, H-Mixer: harmonic mixer, LO: local oscillator, EA: electrical amplifier, ESA: electrical spectrum analyzer, SSA: signal source analyzer, LPF: low pass filter, Freq-C: frequency counter, PID: proportional-integral-derivative controller. **b** Measured RF beatnote spectra of the free-running and stabilized signals, showing a 105,000× improvement of the 3-dB Gaussian linewidth after frequency stabilization at a sweeping time of 39 ms, RBW Resolution bandwidth, VBW Video bandwidth. **c** Frequency noise power spectral

density (PSD) of the RF beatnote down-converted from a frequency-stabilized 651.5 GHz radiation, along with the PSD of local oscillator 1 (LO1), the β -separation line, measured relative laser intensity noise, and flicker frequency noise curve. **d** Allan deviation of the free-running and stabilized terahertz signal along with Allan deviation of the referenced local oscillator (LO2). The stabilized signal shows the relative frequency deviation of $\sigma(\tau) = 1.345 \times 10^{-12} / \tau^{0.95}$. **e** Deterministically tuned terahertz radiation after frequency stabilization over a 14 kHz range, with $\approx 27 \pm 1.5$ Hz discrete tuning steps as shown in inset and only by LO2 frequency resolution.

radiation frequencies and then rolls off to the noise floor of the pyroelectric detector. The detected power above 500 GHz agrees well with the simulated magnitude response of the nanoantenna array denoted with the dashed gray curve. Below 500 GHz, the power deviation arises from spectral filtering as well as degraded terahertz beam coupling inside the pyroelectric detector.

By optimizing the microresonator intracavity power and pump-resonance detuning, the sub-comb lines around the parametric sidebands can be locally excited. Figure 3e shows two example optical cluster frequency comb spectra with the signal-pump frequency spacing of 553 and 651 GHz. The generated frequency comb clusters are subsequently down-converted to the terahertz spectral range to generate multi-frequency terahertz oscillators with line frequency spacing of 19.86 GHz at the 553 and 651 GHz center frequencies. Figures 3f, g show the generated multi-frequency terahertz signal after down-conversion to the RF spectral range via changing the harmonic mixer reference frequency to down-convert all frequency tones simultaneously.

Active feedback stabilization of the generated terahertz radiation

Tunability of the generated single and multi-frequency terahertz wave highly depends on effective microresonator temperature which, in turn, introduces thermal stochastic frequency fluctuations of the generated terahertz signal induced by thermodynamical fluctuations of the microresonator mode. The small mode volume of the microresonator physically leads to high thermal sensitivity to ambient

temperature fluctuations. The thermal instability originates from thermal energy exchange between the microresonator and ambient background or laser heating from the intracavity optical power absorption. The thermal fluctuations, fundamentally mediated by thermal expansion and thermo-refractive index effects, impose phase decoherence of the generated terahertz signal.

The microresonator mode optical frequency is denoted as $\nu_{\mu} = \mu f_{FSR} + f_0$ where f_{FSR} is the mode free spectral range, and f_0 is the offset frequency. To improve the instantaneous linewidth and frequency stability of the generated terahertz signal and further increase its frequency tuning resolution, microresonator intracavity power stabilization (main stabilization loop) and the pump-resonance detuning stabilization (auxiliary stabilization loop) are engaged, as illustrated in Fig. 4a. The frequency tuning resolution is fundamentally limited by the frequency fluctuations of the microresonator FSR, $\Delta f_{FSR}(T)$. With the microresonator thermodynamics⁵⁴, the frequency fluctuations variance behaves as $\langle \Delta f_{FSR}^2 \rangle = |\eta_{FSR}|^2 \frac{k_B T^2}{\rho C V}$ where $\eta_{FSR} = df_{FSR}/dT$ is the thermal transduction coefficient, ρ is the material density, C is the specific heat, and V is the microresonator mode volume. Thermal transduction coefficient can be decomposed via $\eta_{FSR} = \frac{d\nu_{\mu}}{dT} \left(\frac{\partial f_{FSR}}{\partial \nu_{\mu}} + 2 \frac{\partial f_{FSR}}{\partial \delta} \right)$, where ϵ is the mode linewidth⁵⁵. The measured temperature-dependent mode frequency change is $d\nu_{\mu}/dT = 39.2 \text{ GHz/K}$ and $df_{FSR}/d\nu_{\mu} \approx 1/\mu$. To mitigate the thermal noise transduction, $\frac{\partial f_{FSR}}{\partial \nu_{\mu}} + 2 \frac{\partial f_{FSR}}{\partial \delta} = 0$ should be satisfied which requires the stabilization the intracavity power via controlling the pump laser power and frequency.

Discussion

With the terahertz signal generation and active feedback stabilization setup (Fig. 4a), the linearly polarized and power equalized optical beam is injected into the plasmonic nanoantenna array. The generated terahertz signal is down-converted to the RF domain by a harmonic mixer. The detected RF signal is managed by a series of electronics. An electrical spectrum analyzer and a signal source analyzer are used to characterize instantaneous linewidth and frequency noise of the down-converted signal at the intermediate frequency. The measured frequency noise of the down-converted signal is limited by the reference signal (LO1). To facilitate feedback locking, electrical frequency division method is utilized to further decrease the carrier frequency of the down-converted signal which subsequently is referenced to another source (LO2). The timing referenced frequency counter continuously samples the divided signal to examine the frequency stability of the terahertz signal at the free-running and stabilized conditions. The extracted error signal is managed by a proportional-integral-derivative (PID) controller to control the pump laser polarization to stabilize the microresonator intracavity power after polarization demodulation with a linear polarizer. Meanwhile, the integral error signal auxiliary controls pump laser frequency to equivalently stabilize the pump-resonance detuning (δ). We realize a dual-step stabilization protocol including pump laser power locking followed by pump laser frequency locking. Figure 4b shows the free-running and resultant stabilized instantaneous linewidth of the generated terahertz signal. After pump laser power and frequency stabilization, the Gaussian-fitted linewidth is improved $\approx 105,000\times$ for a 39-ms sweep time.

After terahertz signal frequency stabilization, the frequency noise power spectral density (PSD) is measured as shown in Fig. 4c along with the frequency noise of the reference source (LO1), the β separation line, and the flicker frequency noise power law ($1/f$) where the 100-Hz linewidth is observed. The low Fourier frequency flicker noise originates from the pump laser amplifier intensity noise conversion⁵⁶. The instantaneous linewidth and frequency noise PSD characterize the short-term frequency stability. The long-term frequency stability is examined with a referenced frequency counter for a 300-ms gate time (detailed in Methods and Supplementary Information III). Figure 4d shows the Allan deviation of the free-running signal and residual signal at 651.5 GHz. The Allan deviation of the reference signal (LO2) at 4.44841 MHz is included as well. The residual frequency stability is improved by $400,000\times$ for a 1-second averaging time and reaches the instrumental limit of the frequency counter. The stabilized terahertz signal has a frequency tuning range and resolution of 14 kHz and 27 ± 1.5 Hz, respectively (Fig. 4e). The stabilized frequency tuning range is dependent on the feedback locking bandwidth. The frequency tuning resolution is determined by the frequency tuning step of the reference source 2 and bounded by the reference source linewidth and the residual noise of the active feedback locking loop.

We report a chip-scale coherent frequency-agile terahertz radiation synthesizer operating at room temperature based on an integrated microresonator parametric oscillator and a plasmonic nanoantenna array, capable of providing both single-frequency terahertz radiation as well as multi-frequency terahertz oscillators in the same system platform. Through optical-to-terahertz frequency division and without requiring optical spectral shaping, the achieved 2.8-octave frequency tunability is, to our best knowledge, the largest octave range realized in chip-scale semiconductor devices with a single pump laser. Moreover, the ≈ 27 Hz frequency tuning resolution for the 651 GHz carrier frequency is one of the highest resolution achieved to date. With the deterministic pump-resonance laser detuning and hybridized modes with thermal control, we report less than 100 Hz linewidths of the terahertz radiation with feedback stabilization of the microresonator intracavity power. The dual pump power- and frequency-stabilization improves the long-term frequency stability by five orders-of-magnitude, reaching an instrument-limited relative

frequency residual instability of 1×10^{-15} at the averaging time of 1000 s. With our nonlinear parametric oscillation and plasmonic array photomixing, the high-spectral-purity frequency-agile terahertz synthesizer in single-frequency, tunable and multi-frequency realizations enable spectroscopy and waveform synthesis in the terahertz regime, supporting advances in metrology, sensing, frequency-agile imaging and wireless communications.

Methods

Integrated dispersion-managed microresonator fabrication

A 3 μm thick SiO_2 layer is deposited via plasma-enhanced chemical vapor deposition (PECVD) on a *p*-type 8" silicon wafer serving as an under-cladding. Then an 800 nm nitride layer is deposited via low-pressure chemical vapor deposition and patterned by the optimized 248 nm deep-ultraviolet lithography and etched down to the buried oxide cladding via optimized reactive ion dry etching. The etched sidewalls have an etch verticality of 88° characterized by a scanning electron microscope. The nitride rings are then over-cladded with a 4.5 μm thick oxide layer.

Microresonator group velocity dispersion and avoided-mode-crossing characterization

A tunable laser (Santec, TSL-510) is swept over a wavelength range from 1520 to 1610 nm at a sweeping speed of 30 nm/s with an output power of 2 mW to measure the cold cavity mode spectra of the microresonator. The 1% of the laser output power is injected into a fiber coupled hydrogen cyanide gas cell (HCN-13-100, Wavelength References Inc.) to calibrate the cavity mode frequency for extracting the cavity mode group velocity dispersion and wavelength-dependent cavity loaded quality factor. The transmissions of the microresonator and the gas cell are recorded during the laser sweep by a data acquisition system with sampling frequency of 1.7 MHz determined by an unbalanced fiber Mach-Zehnder interferometer (MZI).

Simulated parametric oscillation with Lugiato–Lefever equation

Taking the normal group velocity dispersion (GVD) and avoided mode-crossing into consideration, the tunable optical parametric oscillation dynamics are numerically modeled with the Lugiato–Lefever equation (LLE) written as:

$$t_R \frac{\partial E(t, \tau)}{\partial T} + i \left(\frac{\beta_2}{2} \frac{\partial^2}{\partial \tau^2} - \gamma |E|^2 \right) E(t, \tau) + (\alpha + i\delta) E(t, \tau) = i\sqrt{T} E_{in} \quad (1)$$

where $t_R = 50.3$ ps, $\beta_2 = 18.31$ fs²/mm, $\gamma = 1$ W⁻¹m⁻¹, $Q = 1.55 \times 10^6$, $\alpha = 0.018$, and $T = 0.009$. The pump power P_{in} and wavelength λ_p are set at 1.4 W and 1588 nm. We numerically solve the equation with split-step Fourier method initiating from quantum noise. The tunable parametric oscillation can be excited at the specific microresonator modes by properly setting the avoided-mode frequency shift.

Tunable terahertz wave and multi-frequency terahertz oscillators generation

The generated parametric oscillation with an average power of ≈ 20 dBm is injected into an optical preamplifier after an optical bandpass filter. The amplified optical beam is focused by a biconvex lens with a focus length of 10 cm into the plasmonic nanoantenna array. The generated terahertz signal is collimated and focused by a pair of gold-coated parabolic mirrors. The signal is then received by a harmonic mixer (VDI MixAMC with WR 1.5 and WR 2.2 horn antennas) to down-convert into the RF domain for linewidth and frequency stability examination or by a pyroelectric detector (QMC Instruments Ltd) with a lock-in amplifier (SR830) for terahertz power measurements.

Active stabilization of the terahertz signal

The generated terahertz signal is down-converted to an intermediate frequency (IF) of 1.154 GHz with the harmonic mixer (VDI MixAMC with WR 2.2 horn antenna) referenced to a local oscillator (LO1, Gigatronics 905) at a frequency of LO1 = 12.043 GHz. The IF signal is then amplified by an electrical amplifier (Mini-circuits, ZVA-443HGX+) to ≈ -10 dBm and monitored by an electrical spectrum analyzer (ESA, Agilent MXA9020A). The amplified signal is frequency divided with a $260\times$ RF frequency divider (RF bay, FPS-260-4) to the frequency of 4.44 MHz, which is subsequently filtered out by a low-pass filter (LPF, Mini-circuits, BLP-5+). The divided signal is referenced to the local oscillator 2 (LO2) to obtain phase error signal. The error signal is filtered by another low pass filter (LPF) with a cutoff frequency of 1 kHz and routed to a proportional-integral-differential controller (Vescent photonics, DS-125) to generate feedback signal. The feedback signal controls the pump laser polarization via an electrical-controlled polarization controller (EPC, EOSPACE) combined with a polarization beam splitter to stabilize the intracavity power. Furthermore, the auxiliary of the PID controller is used to control pump laser frequency to equivalently stabilize the pump-resonance detuning.

Data availability

All the data and methods are present in the main text and the supplementary materials. The raw datasets generated during and/or analysed during the current study are available from the corresponding author upon request.

References

- Maestrini, A. et al. A frequency-multiplied source with more than 1 mW of power across the 840–900-GHz band. *IEEE Trans. Microw. Theory Tech.* **58**, 1925–1932 (2010).
- Sengupta, K., Nagatsuma, T. & Mittleman, D. M. Terahertz integrated electronic and hybrid electronic–photonic systems. *Nat. Electron.* **1**, 622–635 (2018).
- Schneider, G. J., Murakowski, J. A., Schuetz, C. A., Shi, S. & Prather, D. W. Radiofrequency signal-generation system with over seven octaves of continuous tuning. *Nat. Photon.* **7**, 118–122 (2013).
- McIntosh, K. A. et al. Terahertz photomixing with diode lasers in low-temperature-grown GaAs. *Appl. Phys. Lett.* **67**, 3844–3846 (1995).
- Berry, C. W., Wang, N., Hashemi, M. R., Unlu, M. & Jarrahi, M. Significant performance enhancement in photoconductive terahertz optoelectronics by incorporating plasmonic contact electrodes. *Nat. Commun.* **4**, 1622 (2013).
- Wang, N., Cakmakyapan, S., Lin, Y. J., Javadi, H. & Jarrahi, M. Room-temperature heterodyne terahertz detection with quantum-level sensitivity. *Nat. Astron.* **3**, 977–982 (2019).
- Khalatpour, A., Paulsen, A. K., Deimert, C., Wasilewski, Z. R. & Hu, Qing High-power portable terahertz laser systems. *Nat. Photon.* **15**, 26–20 (2021).
- Williams, B. S. Terahertz quantum-cascade lasers. *Nat. Photon.* **1**, 517–525 (2007).
- Köhler, R. et al. Terahertz semiconductor-heterostructure laser. *Nature* **417**, 156–159 (2002).
- Chevalier, P. et al. Widely tunable compact terahertz gas lasers. *Science* **366**, 856–860 (2019).
- Choporova, Y. Y. et al. High-power Bessel beams with orbital angular momentum in the terahertz range. *Phys. Rev. A* **96**, 023846 (2017).
- Vijayraghavan, K. et al. Broadly tunable terahertz generation in mid-infrared quantum cascade lasers. *Nat. Commun.* **4**, 2021 (2013).
- Jung, S. et al. Broadly tunable monolithic room-temperature terahertz quantum cascade laser sources. *Nat. Commun.* **5**, 4267 (2014).
- Qin, Q., Williams, B. S., Kumar, S., Reno, J. L. & Hu, Q. Tuning a terahertz wire laser. *Nat. Photon.* **3**, 732–737 (2009).
- Curwen, C. A., Reno, J. L. & Williams, B. S. Broadband continuous single-mode tuning of a short-cavity quantum-cascade VECSEL. *Nat. Photon.* **13**, 855–859 (2019).
- Yang, S.-H. et al. Tunable terahertz wave generation through a novel bimodal laser diode and plasmonic photomixer. *Opt. Express* **23**, 31206–31215 (2015).
- P. N. Butcher and D. Cotter, *The Elements of Nonlinear Optics*. Cambridge University Press, Cambridge, England (1990).
- Preu, S., Döhler, G. H., Malzer, S., Wang, L. J. & Gossard, A. C. Tunable, continuous-wave terahertz photomixer sources and applications. *J. Appl. Phys.* **109**, 061301 (2011).
- Liebermeister, L. et al. Ultra-fast, high-bandwidth coherent cw THz spectrometer for non-destructive testing. *J. Infrared Millim. Terahertz Waves* **40**, 288–296 (2019).
- Stanze, D. et al. Compact cw terahertz spectrometer pumped at 1.5 μm wavelength. *J. Infrared Millim. Terahertz Waves* **32**, 225–232 (2011).
- Nagatsuma, T., Ducournau, G. & Renaud, C. C. Advances in terahertz communications accelerated by photonics. *Nat. Photon.* **10**, 371–379 (2016).
- Koenig, S. et al. Wireless sub-THz communication system with high data rate. *Nat. Photon.* **12**, 977–981 (2013).
- Lu, Q. Y., Wang, F. H., Wu, D. H., Slivken, S. & Razeghi, M. Room temperature terahertz semiconductor frequency comb. *Nat. Commun.* **10**, 2403 (2019).
- Burghoff, D. et al. Terahertz laser frequency combs. *Nat. Photon.* **8**, 462–467 (2014).
- Finneran, I. A. et al. Decade-spanning high-precision terahertz frequency comb. *Phys. Rev. Lett.* **114**, 163902 (2015).
- Yasuaia, T., Kabetani, Y., Saneyoshi, E., Yokoyama, S. & Araki, T. Terahertz frequency comb by multifrequency-heterodyning photoconductive detection for high-accuracy, high-resolution terahertz spectroscopy. *Appl. Phys. Lett.* **88**, 241104 (2006).
- Rösch, M., Scalari, G., Beck, M. & Faist, J. Octave-spanning semiconductor laser. *Nat. Photon.* **9**, 42–47 (2015).
- Gaeta, A. L., Lipson, M. & Kippenberg, T. J. Photonic-chip-based frequency combs. *Nat. Photon.* **13**, 158–169 (2019).
- Huang, S.-W. et al. Globally stable microresonator Turing pattern formation for coherent high-power THz radiation on-chip. *Phys. Rev. X* **7**, 041002 (2017).
- Matsko, A. B., Savchenkov, A. A., Strekalov, D., Ilchenko, V. S. & Maleki, L. Optical hyperparametric oscillations in a whispering-gallery-mode resonator: Threshold and phase diffusion. *Phys. Rev. A* **71**, 033804 (2005).
- Lu, X. et al. Efficient telecom-to-visible spectral translation through ultralow power nonlinear nanophotonics. *Nat. Photon.* **13**, 593–601 (2019).
- Sayson, N. L. B. et al. Octave-spanning tunable parametric oscillation in crystalline Kerr microresonators. *Nat. Photon.* **13**, 701–706 (2019).
- DelHaye, P. et al. Optical frequency comb generation from a monolithic microresonator. *Nature* **450**, 1214–1217 (2007).
- Kippenberg, T. J., Gaeta, A. L., Lipson, M. & Gorodetsky, M. L. Dissipative Kerr solitons in optical microresonators. *Science* **361**, 8083 (2018).
- Yao, B. C. et al. Gate-tunable frequency combs in graphene-nitride microresonators. *Nature* **558**, 410–415 (2018).
- Huang, S. W. et al. Mode-locked ultrashort pulse generation from on-chip normal dispersion microresonators. *Phys. Rev. Lett.* **114**, 053901 (2015).
- Suh, M. G., Yang, Q.-F., Yang, K. Y., Yi, X. & Vahala, K. J. Microresonator soliton dual-comb spectroscopy. *Science* **354**, 600–603 (2016).

38. Marin-Palomo, P. et al. Microresonator-based solitons for massively parallel coherent optical communications. *Nature* **546**, 274–279 (2017).
39. Feldmann, J. et al. Parallel convolutional processing using an integrated photonic tensor core. *Nature* **589**, 52–58 (2021).
40. Xu, X. Y. et al. 11 TOPS photonic convolutional accelerator for optical neural networks. *Nature* **589**, 44–51 (2021).
41. Suh, M. G. & Vahala, K. J. Soliton microcomb range measurement. *Science* **359**, 884–887 (2018).
42. Trocha, P. et al. Ultrafast optical ranging using microresonator soliton frequency combs. *Science* **359**, 887–891 (2018).
43. Riemensberger, J. et al. Massively parallel coherent laser ranging using a soliton microcomb. *Nature* **581**, 164–170 (2020).
44. Jang, Y.-S. et al. Nanometric precision distance metrology via hybrid spectrally-resolved and homodyne interferometry in a single soliton frequency microcomb. *Phys. Rev. Lett.* **126**, 023903 (2021).
45. Spencer, D. T. et al. An optical-frequency synthesizer using integrated photonics. *Nature* **557**, 81–85 (2018).
46. Huang, S. W. et al. A broadband chip-scale optical frequency synthesizer at 2.7×10^{-16} relative inaccuracy. *Sci. Adv.* **2**, e1501489 (2016).
47. Tetsumoto, T. et al. Optically referenced 300 GHz millimetre-wave oscillator. *Nat. Photon.* **15**, 516–522 (2021).
48. B. Wang, et al., Towards high-power, high-coherence, integrated photonic mmWave platform with microcavity solitons. *Light: Sci. Appl.* **10**, (2021).
49. Huang, S.-W. et al. Smooth and flat phase-locked Kerr frequency comb generation by higher order mode suppression. *Sci. Rep.* **6**, 26255 (2016).
50. Kordts, A., Pfeiffer, M. H. P., Guo, H., Brasch, V. & Kippenberg, T. J. Higher order mode suppression in high-Q anomalous dispersion SiN microresonators for temporal dissipative Kerr soliton formation. *Opt. Lett.* **41**, 452–455 (2016).
51. Huang, S.-W. et al. Quasi-phase-matched multispectral Kerr frequency comb. *Opt. Lett.* **42**, 2110–2113 (2017).
52. Copie, F., Conforti, M., Kudlinski, A., Mussot, A. & Trillo, S. Competing Turing and Faraday instabilities in longitudinally modulated passive resonators. *Phys. Rev. Lett.* **116**, 143901 (2016).
53. Turan, D. et al. Wavelength conversion through plasmon-coupled surface states. *Nat. Commun.* **12**, 4641 (2021).
54. Drake, T. E., Stone, J. R., Briles, T. C. & Papp, S. B. Thermal decoherence and laser cooling of Kerr microresonator solitons. *Nat. Photon.* **14**, 480–485 (2020).
55. Stone, J. R. & Papp, S. B. Harnessing dispersion in soliton microcombs to mitigate thermal noise. *Phys. Rev. Lett.* **125**, 153901 (2020).
56. Jeong, D. et al. Ultralow jitter silica microcomb. *Optica* **7**, 1108 (2020).

Acknowledgements

The authors acknowledge fruitful discussions with Dr. Yoonsoo Jang, Prof. Ming Xin, Jaime Gonzalo Flor Flores, Dr. Jinkang Lim, Prof. Heng Zhou, Prof. Shu-Wei Huang, Dr. Jinghui Yang, and Futai Hu on

simulations and general notes. Wong's group acknowledges financial support from the Lawrence Livermore National Laboratory (B622827), the National Science Foundation (1824568, 1810506, 1741707, 1829071), and the Office of Naval Research (N00014-14-1-0041). Jarrahi's group acknowledges financial support from the Office of Naval Research (N00014-19-1-2052). The development of the plasmonic nanoantenna arrays used for photomixing is supported by the Department of Energy (# DE-SC0016925).

Author contributions

W.T.W., M.J., and C.W.W. initiated the project. W.T.W., and P.K.L. conducted the experiments. W.T.W., and P.K.L. analyzed the data and performed the simulations. A.K.V., D.T., J.F.M., and H.L. contributed to the experiments. M.Y. and D.-L.K. performed the device nanofabrication. W.W., P.K.L., M.J., and C.W.W. contributed to writing and revision of the manuscript.

Competing interests

The authors declare no competing interests.

Additional information

Supplementary information The online version contains supplementary material available at <https://doi.org/10.1038/s41467-022-32739-6>.

Correspondence and requests for materials should be addressed to Wenting Wang, Mona Jarrahi or Chee Wei Wong.

Peer review information *Nature Communications* thanks the other, anonymous, reviewer(s) for their contribution to the peer review of this work.

Reprints and permission information is available at <http://www.nature.com/reprints>

Publisher's note Springer Nature remains neutral with regard to jurisdictional claims in published maps and institutional affiliations.

Open Access This article is licensed under a Creative Commons Attribution 4.0 International License, which permits use, sharing, adaptation, distribution and reproduction in any medium or format, as long as you give appropriate credit to the original author(s) and the source, provide a link to the Creative Commons license, and indicate if changes were made. The images or other third party material in this article are included in the article's Creative Commons license, unless indicated otherwise in a credit line to the material. If material is not included in the article's Creative Commons license and your intended use is not permitted by statutory regulation or exceeds the permitted use, you will need to obtain permission directly from the copyright holder. To view a copy of this license, visit <http://creativecommons.org/licenses/by/4.0/>.

© The Author(s) 2022

Supplementary Information

Coherent terahertz radiation with 2.8-octave tunability through chip-scale photomixed microresonator optical parametric oscillation

Wenting Wang^{1,†,*}, Ping-Keng Lu^{2†}, Abhinav Kumar Vinod¹, Deniz Turan², James McMillan¹, Hao Liu¹, Mingbin Yu^{4,5}, Dim-Lee Kwong⁴, Mona Jarrahi^{2,*}, and Chee Wei Wong^{1,*}

¹ Fang Lu Mesoscopic Optics and Quantum Electronics Laboratory, University of California, Los Angeles, CA 90095, United States of America

² Terahertz Electronics Laboratory, University of California, Los Angeles, CA 90095, United States of America

³ State Key Laboratory of Functional Materials for Informatics, Shanghai Institute of Microsystem and Information Technology, Shanghai, China

⁴ Institute of Microelectronics, A*STAR, Singapore 117865, Singapore

[†] These authors contributed equally to this work.

* Email: wentingwang@ucla.edu; mjarrahi@ucla.edu; cheewei.wong@ucla.edu

This Supplementary Information consists of the following sections:

- I. Azimuthal microresonator mode number identification and characterization
- II. Tunable optical parametric sideband and terahertz signal generation experimental setups
- III. Terahertz signal frequency tunability, stability, and comparison with other THz sources.

I. Azimuthal microresonator mode number identification and characterization

Figure S1a shows the setup of the swept-wavelength interferometry where a tunable laser is utilized to measure the transmission of the unbalanced Mach-Zehnder interferometer (MZI), the gas cell, and the microresonator. The frequency response of the unbalanced MZI provides the trigger signal for the data acquisition system to synchronously record the output of the two photodetectors (PD_{Cal} and PD_{Trans}). The frequency of the mode spectra of the microresonator is calibrated by the frequency markers of the gas cell. Figure S1b shows the hybridized mode spectra at the mode-crossing frequency which can be used to indicate the azimuthal mode frequency change. Based on the measured microresonator mode spectra and the transmission of the gas cell, the mode free spectral range is obtained, and the microresonator GVD is fitted with the linear fitting as shown in Figure S1c. Figure S1d shows the extracted loaded quality factor based on the

calibrated cavity frequency and linewidth. The loaded quality factor at the pump mode is 1.55×10^6 and the coupling coefficient is 0.74.

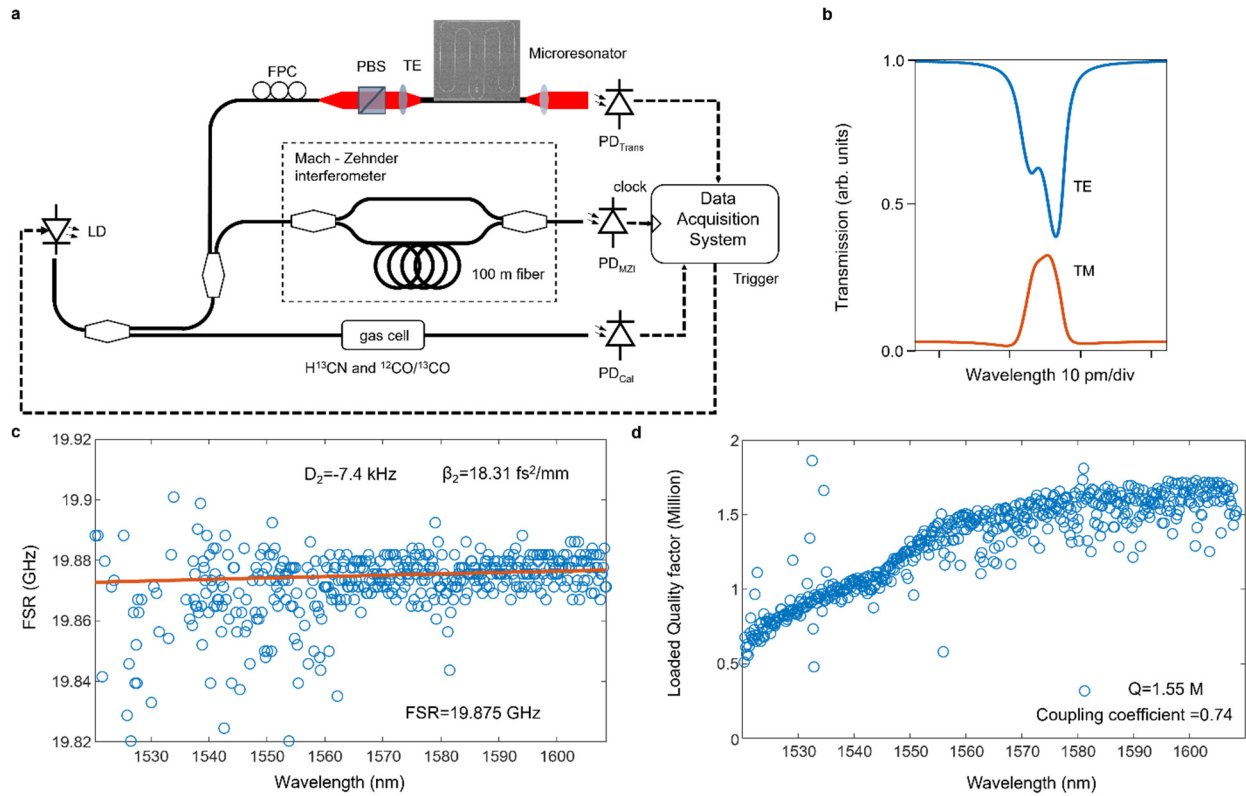


Figure S1 | Microresonator group velocity dispersion characterization setup based on swept-wavelength interferometry. **a**, Experimental setup for the optical transmission measurement of the microresonator to extract the wavelength-dependent quality factor and cavity mode FSR. LD: laser diode, PBS: polarization beam splitter, PD: photodetector, FPC: fiber polarization controller. **b**, Transmission of the TE and TM mode-crossing resonances. **c**, Measured microresonator GVD where $\beta_2 = 18.31 \text{ fs}^2/\text{mm}$. The FSR $\approx 19.875 \text{ GHz}$. **d**, Measured wavelength-dependent loaded cavity quality factor where the loaded quality factor is $Q = 1.55 \times 10^6$ at the pump frequency.

In the microresonator, avoided mode-crossing is observed between TE and TM modes. The two fundamental modes experience an adiabatic crossover and the secondary resonance slowly fades away [S1]. At the crossing position, due to the superposition of the TE and TM mode, the resonance is hybridized. The frequency of the mode-crossing depends sensitively on the temperature of the microresonator [S2, S3]. The experimental setup is shown in Figure S2a where the output of the laser diode is TE-polarized and coupled into the nitride microresonator via a polarization beam splitter with a power extinction ratio of more than 30 dB. A home-made

temperature control unit (TCU) with a Peltier element is used to stabilize chip temperature to maintain the fiber-to-chip coupling. We placed the same PBS to split the TE and TM resonance spectra at the microresonator output. The light at the TE and TM polarizations is fed into two photodetectors (PDA10CF) where the outputs of the PDs are recorded by a data acquisition card simultaneously. Firstly, we increased the pump laser power via a high-power EDFA to observe the mode-pulling effect introduced by the laser heating from optical power absorption inside the nitride waveguide. Secondly, we removed the high-power EDFA and decreased the pump power to eliminate thermal effects. Then, we changed the temperature of the microresonator by controlling the TCU to observe its impact on the mode spectra. Mode-splitting is observed.

Table S1 | Calculation parameters of the avoided mode crossing.

Material parameters, symbol, unit	Parameter value
Intrinsic loss rate of mode A, γ_A	2.45×10^{-5}
Intrinsic loss rate of mode B, γ_B	3.3×10^{-6}
Coupling loss rate of mode A, Γ_A	7×10^2
Coupling loss rate of mode B, Γ_B	1.3×10^{-6}
Coupling strength between mode A and mode B, g_{AB} & g_{BA}	30
coupling loss rates, $\kappa_{A,B}$	1.977

The splitting frequency can be tuned due to the differential thermo-optic effects between the TE and TM modes in the birefringent microresonator. We calculate the amplitude of the splitting mode based on coupled-mode theory [S4] as shown:

$$\frac{dA}{dt} = -(i\omega_A + \gamma_A + \Gamma_A)A - ig_{BA}B - \kappa_A A_{in} \quad (S1)$$

$$\frac{dB}{dt} = -(i\omega_B + \gamma_B + \Gamma_B)B - ig_{AB}A - \kappa_B B_{in} \quad (S2)$$

where ω_A and ω_B are angular mode frequency, γ_A (γ_B) and Γ_A (Γ_B) are the intrinsic and coupling loss rates. g_{BA} and g_{AB} represent the coupling strength between the modes. The mode-splitting frequency is caused by the chip temperature change through $\omega_B - \omega_A = \alpha\Delta T$. The α is related to the difference between the TE and TM thermo-optic coefficients. The coefficients κ_A and κ_B are associated with the coupling loss rates as $\kappa_{A,B} = \sqrt{2\Gamma_{A,B}}$.

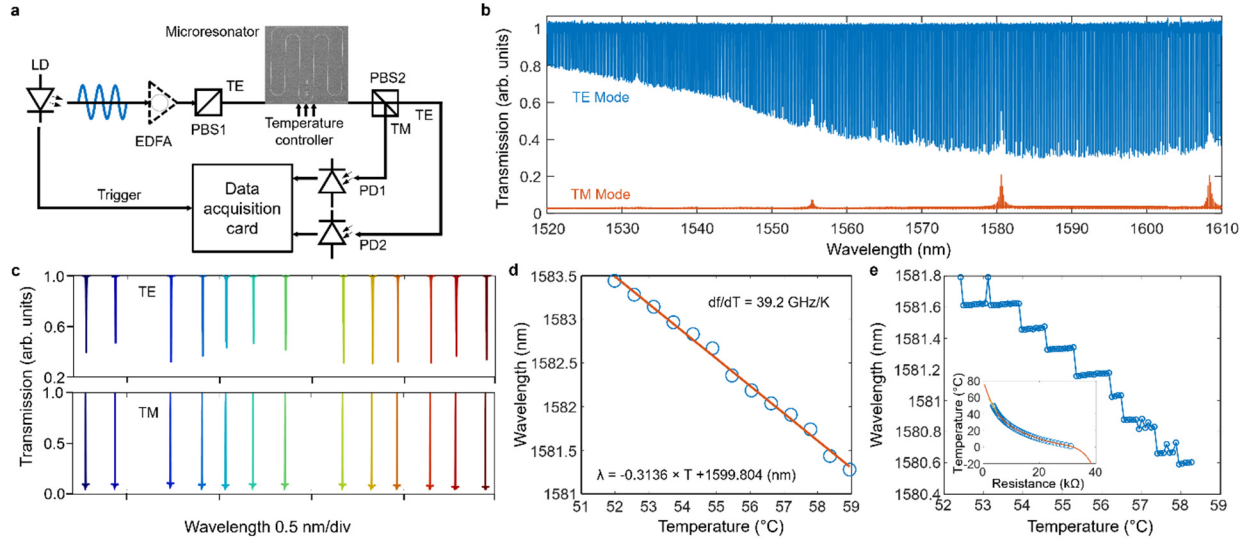


Figure S2 | Avoided mode-crossing and thermal-optic coefficient characterization. a, Experimental setup to examine mode frequency shift and avoided mode-crossing. EDFA: Erbium-doped fiber amplifier. **b,** Transmission of the microresonator at TE and TM polarizations. **c,** TM mode transmission spectra and the corresponding TE mode spectra at the different chip temperature. **d,** Measured TM resonance frequency shift depends on the chip temperature with a tuning step of 0.5 °C. **e,** Measured TM resonance frequency shift via changing the chip temperature with a tuning step of 0.05 °C.

We used the avoided mode-crossing to resolve the azimuthal order ambiguity [S5] of the measured resonances as shown in Figure S2b. The TE transmission optical spectrum shows the three dips with a wavelength separation of 26 nm which is related to the FSR difference between the TE and TM modes. The TM transmission optical spectrum shows the transmission peaks which will be an indicator for the resonant mode pulling. By changing the chip mount temperature, the resonant mode frequency can be tuned through the temperature controller with a resistance step of 0.1 kΩ. Measurements are conducted carefully to avoid temperature fluctuations. Figure S2c shows the measured TE and TM mode pulling by changing temperature. Figure S2d shows the wavelength tuning which shows the resonance wavelength and temperature dependence. Furthermore, we decreased the resistance tuning step to 0.01 kΩ to experimentally demonstrate high-resolution mode pulling as shown in Figure S2e, which shows wavelength variations originating from the temperature fluctuations. Inset is the temperature and the thermistor resistance dependence.

Table S2 | Chip-scale optical parametric oscillation (OPO).

Frequency spacing ($\nu_s - \nu_p$)	Tunability	Tuning method	Material	Nonlinear process	Device	Ref.
142 THz	No	-	Silicon nitride	$\chi^{(3)}$, dFWM	Microring	[S6]
13 THz	Yes	Different resonance	Silicon nitride	$\chi^{(3)}$, FWM-BS	Microring	[S7]
31 THz	No	-	Silicon	$\chi^{(3)}$, dFWM	Nanophotonic wires	[S8]
40.1 THz, 61.4 THz, 81.1 THz	Yes	Different resonance	Magnesium fluoride	$\chi^{(3)}$, dFWM	Microresonator	[S9]
0.64THz, 1.72THz	No	Different microring	Silicon nitride	$\chi^{(3)}$, dFWM	Microring	[S10]
330 GHz to 2.5 THz with 20 GHz frequency tuning step	Yes	Change detuning	Silicon nitride	$\chi^{(3)}$, dFWM	Microring	This work

II. Tunable optical parametric sideband and terahertz signal generation experimental setups

The frequency response bandwidth of the nanoantenna array is calibrated with two free-running tunable lasers. Figure S3a shows the terahertz frequency response calibration setup where the two lasers are combined with a 3-dB fiber coupler and amplified by an L-band optical amplifier. The amplified optical beam is focused on the nanoantenna array with a biconvex lens. The generated terahertz wave is collimated and focused with a pair of parabolic mirrors. At a chopping frequency of 20 Hz, the radiated power is measured using a pyroelectric detector with a lock-in amplifier. The measured power response is shown in Figure S3b, where multiple atmospheric absorption lines are clearly observed. Subsequently we use the nanoantenna array for frequency division of the optical parametric oscillation from mid-infrared to terahertz frequency with the detailed setup shown in Figure S3c. Figure S3d compares the detected intermediate frequency (IF) signals generated using a pair of free-running lasers (blue) and the tunable parametric oscillation (orange), showing a 3.5 \times frequency stability improvement for the latter case.

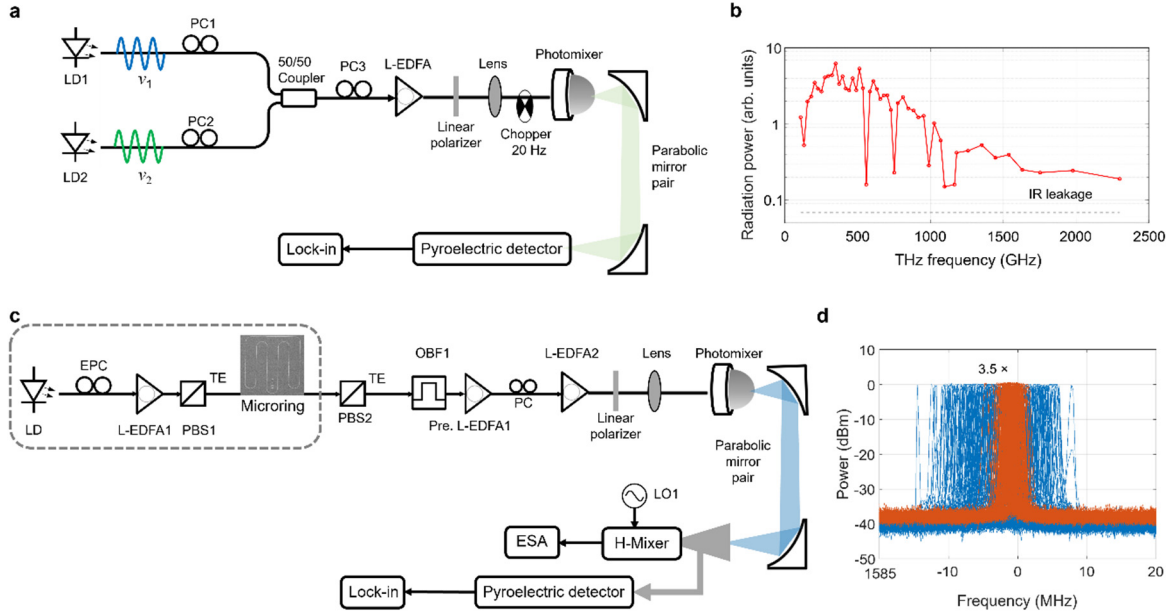


Figure S3 | Plasmonic nanoantenna array characterization with two free-running tunable lasers and the tunable optical parametric oscillation. **a**, Experimental setup to characterize the power response of the plasmonic nanoantenna array. PC: polarization controller, L-EDFA: L-band erbium doped fiber amplifier. **b**, Terahertz power measurement spanning from 100 GHz to 2.3 THz along with the background IR leakage detected by the pyroelectric detector. **c**, Experimental setup for detecting the terahertz radiation generated from the tunable parametric oscillation. OBP: optical bandpass filter, ESA: electrical spectrum analyzer, LO: local oscillator, H-Mixer: harmonic mixer. **d**, Detected intermediate frequency (IF) signal from a terahertz signal generated using a pair of free-running lasers (blue) and the tunable parametric oscillation (orange), showing a 3.5× frequency stability improvement for the latter case.

Figures S4a and S4b show the optical spectra of the pump and tunable parametric oscillation sidebands after power equalization when the resonant mode numbers are 9,500 and 9,501.

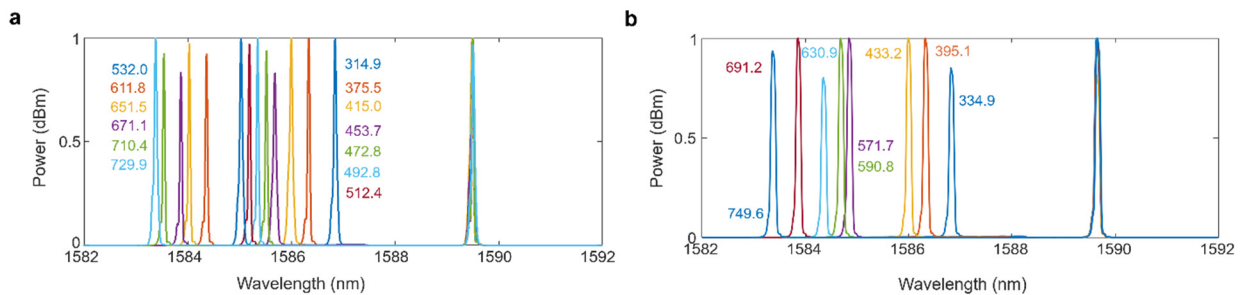


Figure S4 | Tunable optical parametric sideband. **a** and **b**, Measured tunable parametric

sideband when optical pumping the resonance ($\mu' = 9500$) and the adjacent resonance ($\mu' = 9501$). The generated frequencies (in GHz) are marked with the same color as the sidebands.

By properly optimizing the microresonator intracavity power and the pump-resonance detuning, the frequency comb cluster can be excited as shown in Figure S5a with fundamental frequency spacing of ≈ 20 GHz. The cluster optical frequency comb can be downconverted to the terahertz frequency to generate a multi-frequency terahertz oscillator. Moreover, benefiting from the local dispersion, pump-resonance detuning and the microresonator intracavity power control, the cluster frequency comb can be generated with the frequency spacing of double FSR at the different pump-signal frequency spacing as shown in Figures S5b and S5c.

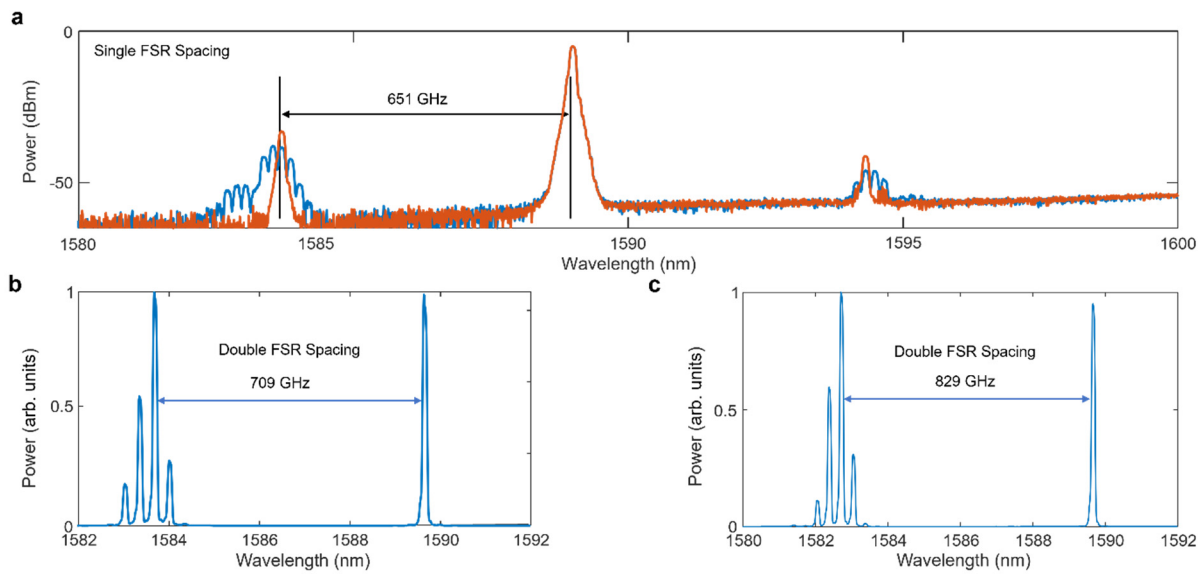


Figure S5 | Tunable optical cluster frequency combs. **a**, Parametric oscillation and the cluster frequency comb generated by controlling the microresonator intracavity power. **b** and **c**, Tunable optical cluster frequency combs for multi-frequency terahertz oscillators generation with pump-signal frequency spacing of 709 and 829 GHz.

III. Terahertz signal frequency tunability, stability, and comparison with other THz sources

The frequency tunability within each resonant mode is investigated by forward and backward adjusting the pump-resonance detuning. The radiation frequency can be tuned over 8.5 and 16.8 MHz as shown in Figures S6a and S6b, which is determined by phase matching condition. Then, we employ the microresonator intracavity power control to stabilize the frequency of the terahertz radiation. Figure S6c shows the frequency fluctuations before and after applying feedback locking, showing a significant improvement on the frequency fluctuations. A timing-referenced frequency

counter is used to evaluate the long-term frequency stability. Figures S6d and S6e present the measured frequency stability of the free-running and stabilized terahertz signals, which shows the root-mean-square (RMS) frequency stability of 1.28 MHz and 0.65 Hz, respectively. The corresponding frequency noise power spectral density of 10^{15} Hz²/Hz (free-running) and 10^3 Hz²/Hz (stabilized) at the Fourier frequency of 100 mHz are also included.

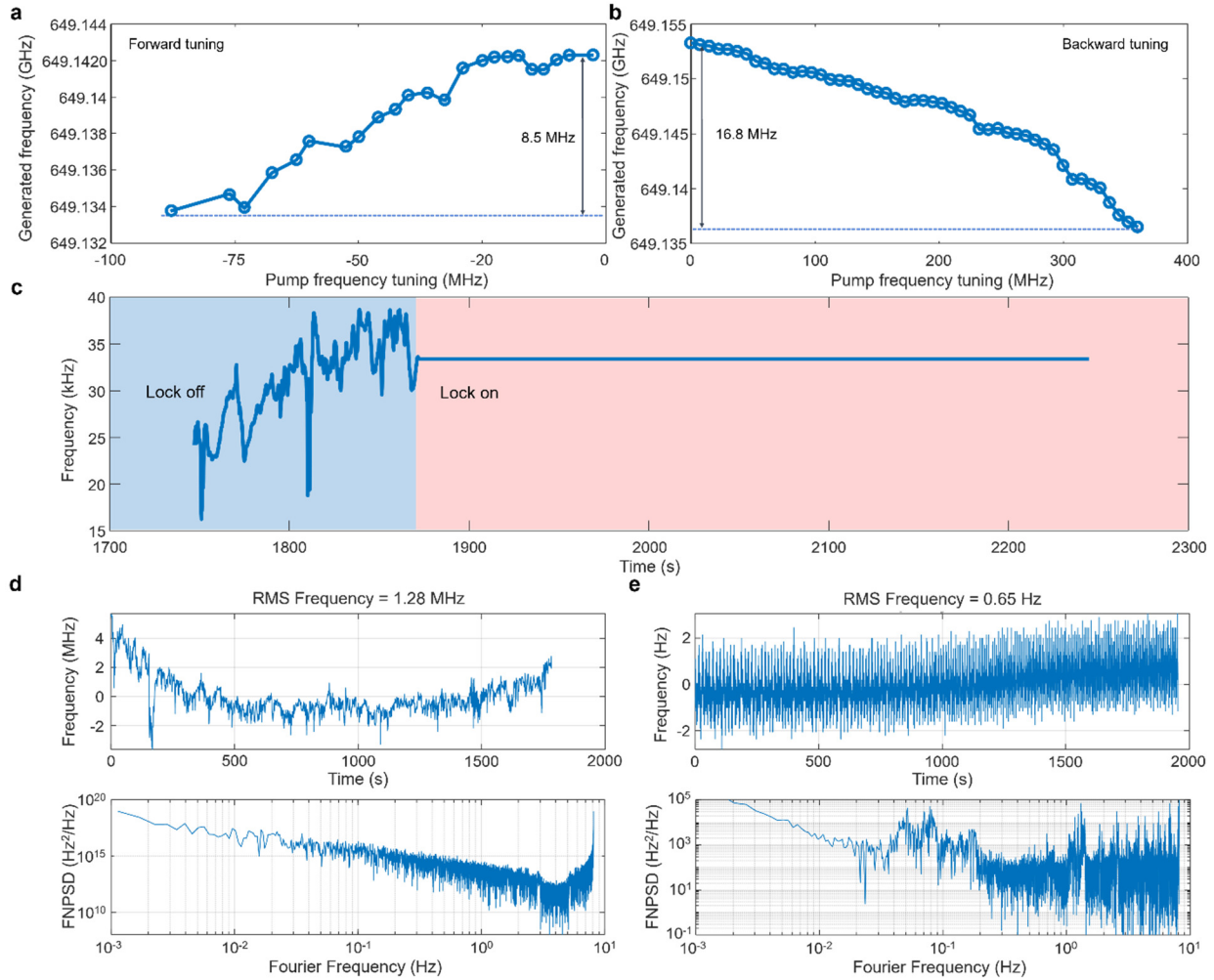


Figure S6 | Terahertz signal frequency tunability and stability. **a** and **b**, Center frequency tuning of the generated terahertz wave by forward- and backward-tuning of the pump laser wavelength, showing ≈ 10 MHz frequency tuning range over microresonator modes. **c**, Frequency locking by feedback control of the microresonator intracavity power showing the terahertz frequency variations before and after locking. **d** and **e**, Frequency fluctuations of the free-running and locked terahertz signal, along with the corresponding frequency noise power spectral density.

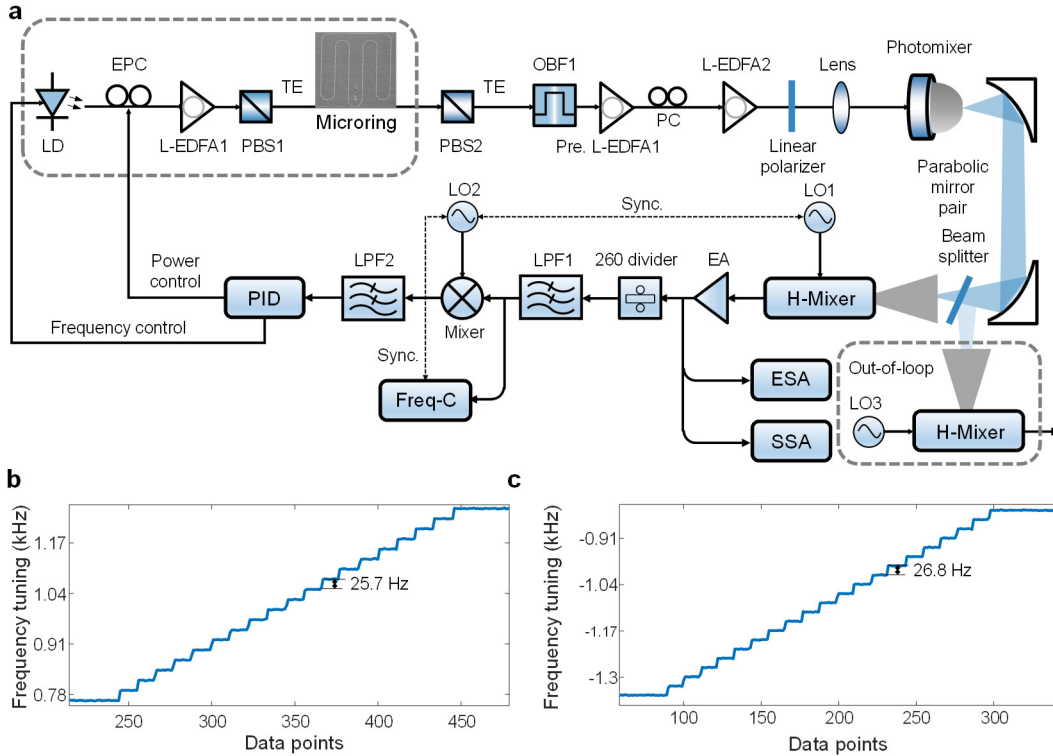


Figure S7 | Out-of-loop frequency tuning measurement. a, Frequency tuning experimental setup. **b,** In loop frequency tuning with a frequency resolution of 25.7 Hz at the carrier of 651.5 GHz. **c,** Out-of-loop frequency tuning with a frequency resolution of 26.8 Hz at the carrier of 651.5 GHz.

Figure S8 shows an example intensity fluctuation characterization with a harmonic mixer, of an optically generated 651.5 GHz signal. Due to the fast frequency fluctuations, we utilize an electrical spectral analyzer to examine the amplitude noise distribution and peak power fluctuations based on 200 measurements in the free-running condition as shown in Figure S8c. In the free-running measurement, we observe that amplitude noise reaches to the instrument-limit as shown in Figure S8b. After phase-locking the 651.5 GHz signal, we use the signal source analyzer to examine its frequency noise where we observe the characteristic noise features from the reference local oscillator and the pump laser intensity noise conversion. Since the nanoantenna array operates without any bias voltage, the direct current through the emitter is eliminated, leading to minimal heating. Consequently, the shot noise and thermal noise contribution from the nanoantenna array itself is believed to be negligible under our experimental conditions. Therefore, when the plasmonic nanoantenna array converts the incident optical frequencies into a terahertz

wave at the beat frequency, the terahertz frequency noise is dominated by the laser noise in our approach.

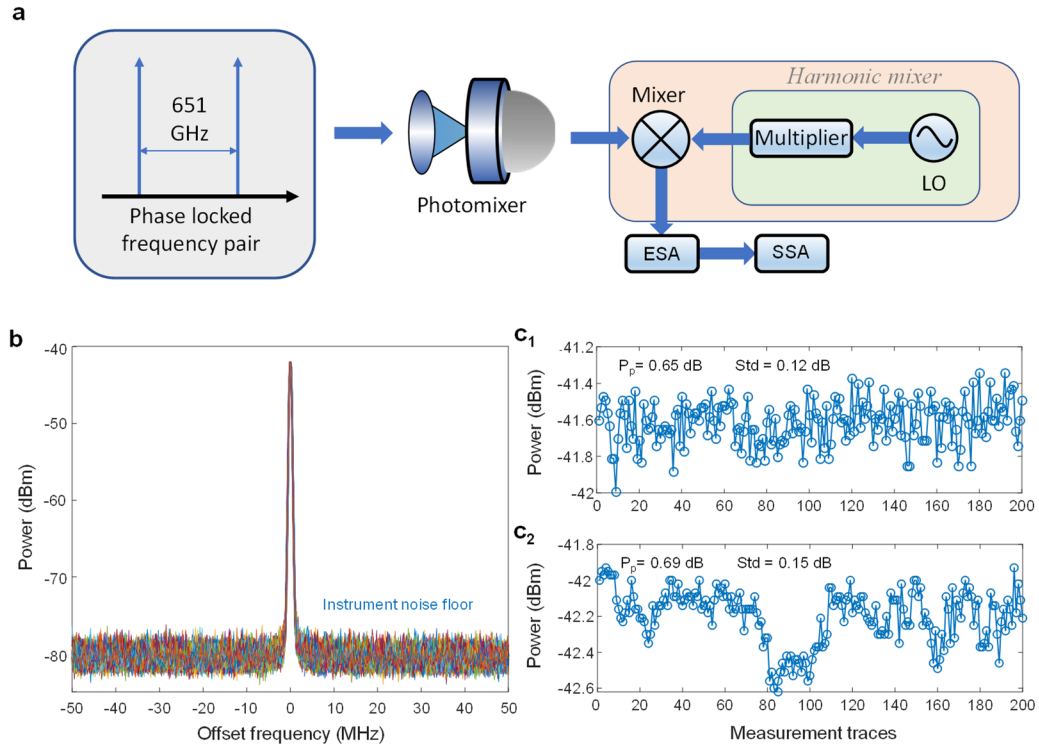


Figure S8 | Intensity fluctuation characterization with a harmonic mixer. **a**, Illustration of intensity and frequency noise characterization setup. **b**, RF spectral traces with continuous measurements for the phase coherent terahertz radiation after removing free-running frequency fluctuations. **c₁** and **c₂**, RF signal peak power continuous sampling for a laser pair and a phase-locked parametric oscillation.

In Table S3, we summarize the different terahertz radiation sources using integrated fully electronic, and hybrid electronic-photonic systems based on different semiconductor substrates for comparison.

Table S3 | State-of-the-art terahertz radiation sources across electronics, photonics and hybrid approaches.

Maximum frequency (f_{\max}) and frequency tuning range (f_t)	Tunability (tuning step)	Linewidth	Radiation power (CW)	Material	Size	Method	Ref.
$f_{\max} = 1.5$ THZ $f_t = 0.61$ THZ	Yes	-	-	InP	8 μm	25-nm InP HEMT	[S11]
$f_{\max} < 1.1$ THZ $f_t < 0.52$ THZ	Yes	-	$> 50 \text{ mW}/\mu\text{m}^2$	InP	< 6 μm	InP DHBT	[S12]
$f_{\max} = 2.7$ THZ	Yes	> 100 MHz	18 μW	-	-	Schottky Diode	[S13]

$f_t = 0.2$ THz							
$f_{\max} = 1.33$ THz $f_t = 0.15$ THz	Yes	-	5.3 μ W	-	0.39 mm ²	MOS-VAR	[S14]
$f_{\max} = 0.55$ THz $f_t = 0.01$ THz	Yes	Phase noise: -79 dBc/Hz	> 61 μ W	Silicon	2.16 mm ²	TPCVCO	[S15]
$f_{\max} = 0.12$ THz $f_t = 0.11$ THz	Yes	150 kHz	100 μ W	Silicon-InP	-	Dual Tunable Lasers	[S16]
$f_{\max} = 2.25$ THz $f_t = 1.92$ THz	Yes	12 kHz	10 nW	InP-Polymer	-	Dual Tunable DBR laser	[S17]
$f_{\max} = 0.5$ THz $f_t = 0.2$ THz	Yes	-	3.2 μ W	-	-	Spectral Shaping Frequency Comb	[S18]
$f_{\max} = 0.32$ THz $f_t = 0.22$ THz	No	-	3.3 mW	SiGe	2.1 mm ²	Coupled Harmonic Oscillators	[S19]
300 GHz	No	-	-	-	-	UTC-PD	[S20]
99.75 GHz	No	-	5 mW	-	-	High-speed PD	[S21]
1.14 THz, 1.28 THz, 1.43 THz, 1.57 THz	Yes	9 kHz	600 μ W	ErAs:In GaAs	-	DC-biased Plasmonic Photomixer	[S10]
$f_{\max} = 2.5$ THz $f_t = 2.2$ THz	Yes (20 GHz, 27 Hz)	100 Hz	10 μ W	InAs	-	Plasmonic Photomixer	This work

HEMT: high electron mobility transistor; DHBT: double heterojunction bipolar transistor; MOSFET: Metal oxide semiconductor field-effect transistor; UTC-PD: uni-travelling-carrier photodiode; MOS-VAR: Metal oxide semiconductor varactors; TPCVCO: triple-pushed Colpitts voltage controlled oscillator.

Supplementary References

- S1. Y. Liu, Y. Xuan, X. X. Xue, P. H. Wang, S. Chen, A. J. Metcalf, J. Wang, D. E. Leaird, M. H. Qi, and A. M. Weiner, Investigation of mode coupling in normal-dispersion silicon nitride microresonators for Kerr frequency comb generation. *Optica* **1**, 137-144 (2014).
- S2. X.X. Xue, Y. Xuan, C. Wang, P.-H. Wang, Y. Liu, B. Niu, D.E. Leaird, M.H. Qi, and A.M. Weiner, Thermal tuning of Kerr frequency combs in silicon nitride microring resonators. *Opt. Express* **24**, 687-698 (2016).
- S3. K. Ikeda, R. E. Saperstein, N. Alic, and Y. Fainman, Thermal and Kerr nonlinear properties of plasma-deposited silicon nitride/ silicon dioxide waveguides. *Opt. Express* **16**, 12987-12994 (2008).
- S4. W. L. Wang and A. N. Luiten, Mode-interactions and polarization conversion in a crystalline microresonator. *Opt. Lett.* **40**, 5431-5434 (2015).
- S5. A.W. Elshaari, I. E. Zadeh, K. D. Jöns, and V. Zwiller, Thermo-optic characterization of silicon nitride resonators for cryogenic photonic circuits. *IEEE Photonics J.* **8**, 2701009 (2016).

- S6. X. Lu, G. Moille, Q. Li, D. A. Westly, A. Singh, A. Rao, S.-P. Yu, T. C. Briles, S. B. Papp, and K. Srinivasan, Efficient telecom-to-visible spectral translation through ultralow power nonlinear nanophotonics. *Nature Photon.* **10**, 406–414 (2016).
- S7. Q. Li, M. Davanço, and K. Srinivasan, Efficient and low-noise single-photon-level frequency conversion interfaces using silicon nanophotonics. *Nature Photon.* **10**, 406–414 (2016).
- S8. X. Liu, B. Kuyken, G. Roelkens, R. Baets, R. M. Osgood Jr, and W. M. J. Green, Bridging the mid-infrared-to-telecom gap with silicon nanophotonic spectral translation. *Nature Photon.* **6**, 667–670 (2012).
- S9. N. L. B. Sayson, T. Bi, V. Ng, H. Pham, L. S. Trainor, H. G. L. Schwefel, S. Coen, M. Erkintalo, and S. G. Murdoch, Octave-spanning tunable parametric oscillation in crystalline Kerr microresonators. *Nature Photon.* **13**, 701–706 (2019).
- S10. S.-W. Huang, J. Yang, S.-H. Yang, M. Yu, D.-L. Kwong, T. Zelevinsky, M. Jarrahi, and C. W. Wong, Globally stable microresonator Turing pattern formation for coherent high-power THz radiation on-chip. *Phys. Rev. X* **7**, 041002 (2017).
- S11. X. Mei, W. Yoshida, M. Lange, J. Lee, J. Zhou, P.-H. Liu, K. Leong, A. Zamora, J. Padilla, S. Sarkozy, R. Lai, and W. R. Deal, First demonstration of amplification at 1 THz using 25-nm InP high electron mobility transistor process. *IEEE Electron Dev. Lett.* **36**, 327–329 (2015).
- S12. M. Urteaga, R. Pierson, P. Rowell, V. Jain, E. Lobisser, and M. J. W. Rodwell, 130 nm InP DHBTs with $f_t > 0.52$ THz and $f_{max} > 1.1$ THz. *In Proc. 69th Annu. Device Res. Conf.* 281–282 (2011).
- S13. A. Maestrini, I. Mehdi, J. V. Siles, R. Lin, C. Lee, G. Chattopadhyay, J. Pearson, and P. Siegel, Frequency tunable electronic sources working at room temperature in the 1 to 3 THz band. *Proc. SPIE 8496*, 84960F (2012).
- S14. Z. Ahmad, M. Lee and K. O. Kenneth, 1.4 THz, -13 dBm-EIRP frequency multiplier chain using symmetric- and asymmetric-CV varactors in 65 nm CMOS. *IEEE Int. Solid State Circuits Conf.* 350–351 (2016).
- S15. Y. Zhao, H.-C. Lu, H.-P. Chen, Y.-T. Chang, R. Huang, H.-N. Chen, C. Jou, F.-L. Hsueh, and M.-C. F. Chang, A 0.54–0.55 THz 2×4 coherent source array with EIRP of 24.4 dBm in 65nm CMOS technology. *IEEE MTT-S Int. Microw. Symp.* 1–3 (2015).

- S16. J. Hulme, M. Kennedy, R.-L. Chao, L. Liang, T. Komljenovic, J.-W. Shi, B. Szafraniec, D. Baney, and J. E. Bowers, Fully integrated microwave frequency synthesizer on heterogeneous silicon- III/V. *Opt. Express* **25**, 2422–2431 (2017).
- S17. G. Carpintero, S. Hisatake, D. D. Felipe, R. Guzman, T. Nagatsuma, and N. Keil, Wireless data transmission at terahertz carrier waves generated from a hybrid InP-polymer dual tunable DBR laser photonic integrated circuit. *Sci. Rep.* **8**, 3018 (2018).
- S18. X. Pang, S. Jia, O. Ozolins, X. Yu, H. Hu, L. Marcon, P. Guan, F. Da Ros, S. Popov, G. Jacobsen, M. Galili, T. Morioka, D. Zibar, and L. K. Oxenløwe, 260 Gbit/s photonic–wireless link in the THz band. *In Proc. 2016 IEEE Photon. Conf.* 1–2 (2016).
- S19. R. Han, C. Jiang, A. Mostajeran, M. Emadi, H. Aghasi, H. Sherry, A. Cathelin, and E. Afshari, A SiGe terahertz heterodyne imaging transmitter with 3.3 mW radiated power and fully-integrated phase-locked loop. *IEEE J. Solid State Circuits*, **50**, 2935–2947 (2015).
- S20. T. Tetsumoto, T. Nagatsuma, M. E. Fermann, G. Navickaite, M. Geiselmann, and A. Rolland, Optically referenced 300 GHz millimetre-wave oscillator. *Nature Photon.* **15**, 516–522 (2021).
- S21. B. Wang, J. S Morgan, K. Sun, M. Jahanbozorgi, Z. Yang, M. Woodson, S. Estrella, A. Beling, and X. Yi, Towards high-power, high-coherence, integrated photonic mmWave platform with microcavity solitons. *Light: Sci. Appl.* **10**, (2021).